ACS APPLIED ENERGY MATERIALS

www.acsaem.org
Article

Construction of Metal-Coordinated Bipyridine-Based Conjugated Microporous Polymers as Robust Electrocatalysts for Hydrogen Evolution

Tapomay Mondal,[#] Mohamed Gamal Mohamed,*,[#] Ahmed A. K. Mohamed, and Shiao-Wei Kuo*

Cite This: ACS Appl. Energy Mater. 2025, 8, 7703−7713
Read Online

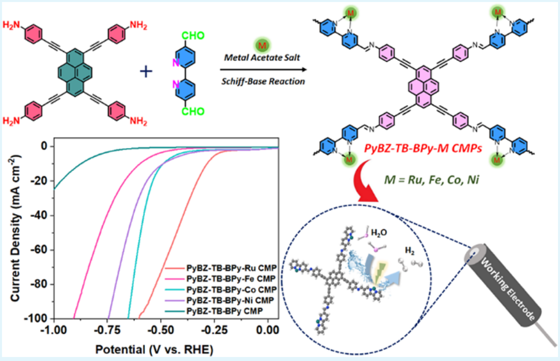

ABSTRACT: Employing water splitting (WS) to develop electrocatalysts for the hydrogen evolution reaction (HER) presents a promising strategy for generating cost-effective energy. In recent years, extensive research has focused on designing metal-based conjugated microporous polymers (CMPs) catalysts with abundant electrocatalytically active sites, offering an efficient substitute for precious metal-based Pt/C catalysts. In this study, a series of microporous pyrene-metal CMPs (Ru, Fe, Co, and Ni) were synthesized via a one-pot Schiff-base [4 + 2] condensation reaction between 4,4',4'',4'''-(pyrene-1,3,6,8-tetrayltetrakis(ethyne-2,1-diyl))-tetraaniline [PyBZ-TB-4NH$_2$] and [2,2'-bipyridine]-5,5'-dicarbaldehyde [BPy-2CHO] in the presence of different derivatives of transition metal salts (Ru, Fe, Co, Ni) to afford PyBZ-TB-BPy-M CMPs. The uncoordinated PyBZ-TB-BPy CMP and coordinated PyBZ-TB-BPy-M CMPs were investigated for their electrochemical HER performance. Notably, PyBZ-TB-BPy-Ru CMP exhibited an impressively minimal overpotential of 285 mV (at 10 mA cm^{-2}) and a charge transfer resistance (R_{ct}) of 245 Ω at 280 mV overpotential in 1 M KOH electrolyte. Furthermore, PyBZ-TB-BPy-Ru CMP demonstrated excellent stability, maintaining its electrocatalytic activity with minimal performance degradation after 18 h of chronoamperometry. Additionally, PyBZ-TB-BPy-Fe, PyBZ-TB-BPy-Co, and PyBZ-TB-BPy-Ni CMPs displayed enhanced electrocatalytic activity compared to the PyBZ-TB-BPy CMP. The exceptional performance of these metal-coordinated PyBZ-TB-BPy-M CMPs highlights their potential as cost-effective, low-resistance electrocatalysts with highly exposed active sites for efficient alkaline HER.

KEYWORDS: *pyrene, bipyridine, conjugated microporous polymers, electrocatalyst, hydrogen evolution reaction*

INTRODUCTION

Excessive reliance on fossil fuels has severely impacted all life on earth, contributing to critical issues such as climate change and the greenhouse effect.[1−5] As a result, the development of clean, renewable, and cost-effective energy sources has become a pressing global challenge.[6−10] Hydrogen (H_2) is considered an ideal energy carrier due to its high gravimetric energy density and environmentally friendly combustion byproduct.[11−17] Electrocatalytic WS is one of the most encouraging strategies for generating H_2 as a sustainable energy source.[18,19] Consequently, the advancement of efficient electrocatalysts for the HER is essential for the widespread adoption of clean hydrogen energy.[20] Although platinum (Pt) is the most effective catalyst for HER, its high cost and scarcity limit its large-scale application.[21] As a viable alternative, metallic ruthenium (Ru) has demonstrated favorable hydrogen adsorption properties during the HER process while offering a significant economic advantage over Pt-based materials.[22,23] However, noble metal nanoparticles, due to their small size, are susceptible to agglomeration during catalytic processes, which can hinder their stability and efficiency.[24]

Researchers have also found that compounds of earth-abundant metals such as Fe, Co, Ni, and Mo demonstrate promising performance for the HER in alkaline electrolytes[25−28] However, these materials often suffer from limited selectivity, poor durability, and a high susceptibility to gas poisoning.[29] To address these challenges, there is growing interest in developing stable catalysts with abundant electrochemically active sites. A key strategy involves minimizing the loss of precious metal sites and preventing leaching during reactions. To enhance stability and performance, these catalysts are typically supported on specific materials during their preparation.

Received: April 5, 2025
Revised: May 5, 2025
Accepted: May 12, 2025
Published: May 19, 2025

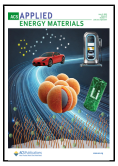

https://doi.org/10.1021/acsaem.5c00992

In recent decades, extensive research has identified transition metal-based nitrides, sulfides, phosphides, carbides, chalcogenides, and various compounds and alloys as potential electrocatalysts for efficient performance in HER application.[30−33] Despite these advancements, the design of highly effective electrocatalysts with enhanced activation energy, fast reaction kinetics, and prolonged stability remains a crucial objective in pursuing sustainable energy solutions. CMPs have garnered substantial attention due to their extended π-conjugation frameworks, structural tunability, adjustable energy band structures, high specific surface area, low density, and excellent stability.[34−44] The high specific surface area of these materials can facilitate mechanical energy capture, while their intrinsic flexibility and deformability may enhance their sensitivity in mechanical energy harvesting applications[45,46] To address the challenge of sluggish reaction kinetics in overall water splitting, optimizing the CMP structure can enable the formation of suitable energy bands that meet the thermodynamic requirements for overall water splitting while also enhancing charge migration and separation.[47] Furthermore, CMPs have been investigated for their potential in various applications, such as energy storage, chemical sensing, and electrocatalysis, highlighting their adaptability and promise in diverse energy-related and analytical technologies.[37,38,38,39,39−49]

Previous studies have shown that the electrocatalytic performance of carbonaceous materials can be significantly improved through single or dual heteroatom doping with elements such as nitrogen, sulfur, phosphorus, or boron.[50−52] Among various porous carbonaceous materials, CMPs have emerged as promising candidates for demands in gas adsorption, energy storage, and catalysis due to their cost-effectiveness, high surface area, and facile synthesis.[38,39,53−56] Additionally, CMPs serve as excellent precursors for the fabrication of heteroatom-doped porous carbons with enhanced HER activity. Recently, Das et al. synthesized Ni(II)- and Cu(II)-embedded porphyrin-pyrene-based CMPs, achieving low overpotentials of 213 mV and 250 mV, respectively, to reach 10 mA cm^{-2} for HER.[27] Similarly, Jia et al. developed a cobalt porphyrin-based CMP that exhibited HER catalytic activity at an overpotential of 360 mV for 10 mA cm^{-2}.[57] But as far as we know, the correlation between structure and function of metal (Ru, Fe, Co, and Ni) coordinated with PyBZ-TB-BPy CMP electrode systems as electrocatalysts for the HER has yet to be fully elucidated.

Herein, we report a scalable and straightforward strategically incorporating bipyridine (BPy) units as coordinating ligands into an imine-based CMP, PyBZ-TB-BPy CMP, through a Schiff-base [4 + 2] condensation reaction between PyBZ-TB-4NH$_2$ and BPy-2CHO. Building upon this framework, we further synthesized a series of novel porous metal-coordinated PyBZ-TB-BPy-M CMPs by employing the same Schiff-base reaction in the presence of transition metal salts (Ru, Fe, Co, and Ni). This approach facilitated the formation of robust electrocatalysts for the HER through the direct coordination of PyBZ-TB-4NH$_2$ and BPy-2CHO with acetate salts of Ru, Fe, Co, and Ni, demonstrating a promising route for the development of efficient and durable HER catalysts. The molecular architecture, porosity, thermal stability, and surface morphology of PyBZ-TB-BPy CMP and its metal-coordinated derivatives were systematically investigated and critically analyzed in depth through FTIR, TGA, SEM, XPS, and SEM-EDS mapping. Compared to PyBZ-TB-BPy CMP, PyBZ-TB-BPy-Fe CMP, PyBZ-TB-BPy-Co CMP, PyBZ-TB-BPy-Ni CMP, and other porous polymer-based catalysts, the electrochemical analysis revealed that the PyBZ-TB-BPy-Ru CMP electrocatalyst exhibited outstanding performance for the HER. It achieved an impressively low overpotential of 285 mV at a current density of 10 mA cm^{-2}, along with a remarkably low charge transfer resistance (R_{ct}) of 245 Ω at an overpotential of 280 mV in alkaline media, underscoring its superior catalytic efficiency and potential for sustainable H_2 production. This study definitively demonstrates that electron-transferable transition metals [Ru, Fe, Co, and Ni], when coordinated within the PyBZ-TB-BPy CMP framework, can effectively drive overall water splitting in an alkaline medium, highlighting their immense potential for efficient and sustainable H_2 production.

EXPERIMENTAL SECTION

Materials. Potassium carbonate (K_2CO_3), 1,2-dichlorobenzene (1,2-DCB), n-butanol (*n*-BuOH), iron(II) acetate [$Fe(CH_3COO)_2$], pyrene, 1,4-dioxane (DO), cobalt(II) acetate [$Co(CH_3COO)_2$], nickel(II) acetate tetrahydrate [$Ni(CH_3COO)_2.4H_2O$], ruthenium(II) acetate [$Ru(CH_3COO)_2$], $Pd(PPh_3)_4$, methanol (MeOH), acetic acid (AcOH), [2,2'-bipyridine]-5,5′-dicarbaldehyde [BPy-2CHO], 4-ethynylaniline [4-TB-PhNH$_2$], were ordered from Sigma-Aldrich and Acros. 1,3,6,8-tetrabromopyrene (Py-4Br) was synthesized according to methods described in prior literature.[58−61]

Synthesis of PyBZ-TB-4NH$_2$. In a 50 mL round-bottom flask, 4-TB-PhNH$_2$ (4.06 g, 34.8 mmol), $Pd(PPh_3)_4$ (0.23 g, 0.06 mmol), and CuI (0.06 g, 0.29 mmol) and Py-4Br (3 g, 5.8 mmol) were combined. Next, DMF (81 mL) and Et_3N (35 mL) were poured. The mixture was degassed through three freeze−pump−thaw cycles, purged with N_2, and then stirred at 110 °C overnight. The reaction mixture was with water. The resulting residue was washed with water and recrystallized in DO, yielding an orange powder (2.84 g). FTIR (cm^{-1}, Figure S1): 3378, 3210 (NH$_2$), 3034, 2197 (C≡C). ^{1}H NMR (δ, Figure S2): 8.5, 8.03, 7.3, 6.5, 5.5 (NH$_2$) ppm. ^{13}C NMR (Figure S3): 149.9, 133.1, 131.6, 129.9, 128.7, 126.3, 119.2, 114.1, 113.7, 98.6 (C≡C) and 85.2 (C≡C) ppm. T_{d5} = 326.5 °C [Figure S4].

Synthesis of PyBZ-TB-BPy CMP. In a 25 mL Pyrex tube, 1,2-DCB (7 mL), *n*-BuOH (7 mL), BPy-2CHO (24 mmol), and PyBZ-TB-4NH$_2$ (12 mmol) were combined. The mixture was subjected to sonication for 5 min, and added 1.5 mL of 6 M AcOH. To ensure thorough degassing, three freeze−pump−thaw cycles were performed, after which the mixture underwent an additional 5 min of sonication and Ar purging and subsequently heated at 125 °C for 5 days. The resulting solid was collected by filtration, meticulously washed with DMF, DCM, and MeOH, and vacuum-dried to yield a dark red powder.

Synthesis of PyBZ-TB-BPy-Ru, PyBZ-TB-BPy-Fe, PyBZ-TB-BPy-Co, and PyBZ-TB-BPy-Ni CMPs. In a 25 mL Pyrex tube, $Ru(CH_3COO)_2$ (24 mmol) or $Fe(CH_3COO)_2$ (24 mmol), or $Co(CH_3COO)_2$ (24 mmol), or $Ni(CH_3COO)_2$ (24 mmol), 1,2-DCB (8 mL), *n*-BuOH (8 mL), BPy-2CHO (24 mmol), and PyBZ-TB-4NH$_2$ (12 mmol) were combined. The mixture was first sonicated for 5 min and 1.5 mL of 6 M AcOH. To achieve thorough degassing, three freeze−pump−thaw cycles were conducted. The mixture then underwent an additional 5 min of sonication and Ar purging before being heated at 125 °C for 3 days. Upon cooling to room temperature, the solid was collected via filtration, thoroughly washed with DMF, DCM, and MeOH to eliminate any unreacted salts and monomers, and subsequently vacuum-dried to afford a dark brown solid for PyBZ-TB-BPy-Ru CMP, a red solid for PyBZ-TB-BPy-Fe CMP, a dark brown solid for PyBZ-TB-BPy-Co CMP, and a red powder for PyBZ-TB-BPy-Ni CMP.

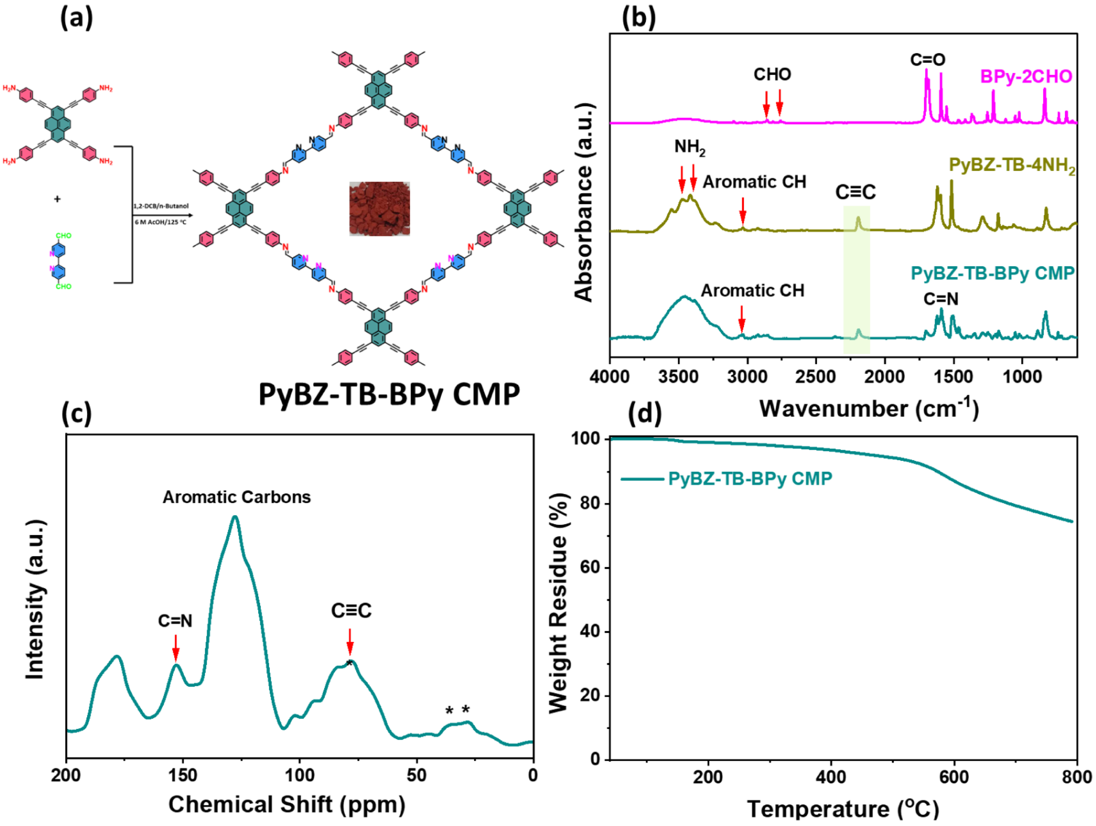

Figure 1. (a) Schematic representation of PyBZ-TB-BPy CMP synthesis, (b) FTIR spectra of PyBZ-TB-4NH$_2$, BPy-2CHO, and PyBZ-TB-BPy CMP, (c) solid-state ^{13}C NMR analysis, and (d) TGA thermogram of PyBZ-TB-BPy CMP.

■ RESULTS AND DISCUSSION

Synthesis and Characterization of PyBZ-TB-BPy CMP. The N,N'-chelating site of BPy-2CHO enables it to coordinate effectively with metal ions, forming stable five-membered rings and robust coordination complexes.[39] To synthesize an imine-linked CMP, [2,2'-bipyridine]-5,5′-dicarbaldehyde (BPy-2CHO) and PyBZ-TB-4NH$_2$, a tetraamine-functionalized precursor, were employed as the key building blocks. Following 5 days of continuous heating and vigorous stirring in an acidic medium, PyBZ-TB-4NH$_2$ and BPy-2CHO underwent a Schiff-base [4 + 2] condensation reaction in a 1,2-DCB/*n*-BuOH solvent system, resulting in the formation of a robust PyBZ-TB-BPy CMP as a dark red powder [Figure 1a]. Fourier-transform infrared (FT-IR) spectroscopy was applied to systematically analyze the structural evolution of PyBZ-TB-BPy CMP by comparing it with its respective precursors, PyBZ-TB-4NH$_4$ and BPy-2CHO, to monitor functional group transformations. As illustrated in Figure 1b, the successful formation of imine linkages in PyBZ-TB-BPy CMP is confirmed by the appearance of a distinct C = N stretching vibration at 1601 cm^{-1}. Additionally, the significant attenuation of the aldehyde-related absorption bands at 2843, 2751, and 1697 cm^{-1} (C = O unit), along with the complete disappearance of the amino group signals at 3478−3401 cm^{-1}, further substantiates the effective condensation reaction and the structural integrity of the synthesized PyBZ-TB-BPy CMP.[62,63] Also, the structural integrity of PyBZ-TB-BPy CMP was unequivocally confirmed by its ^{13}C solid-state NMR spectrum [Figure 1c]. The resonance peaks observed between 104 and 137 ppm correspond to the phenyl carbon framework of PyBZ-TB-BPy CMP, while the characteristic peaks at 83.6 and 77.3 ppm are ascribed to the carbon in the C≡C bond. Additionally, the Schiff-base C = N bond is distinctly represented by a peak at approximately 154 ppm, further substantiating the successful formation of PyBZ-TB-BPy CMP. These findings provide compelling evidence that the PyBZ-TB-BPy CMP was effectively synthesized through Schiff-base condensation, establishing robust C = N linkages within the conjugated framework. Thermogravimetric analysis (TGA) confirms the exceptional thermal stability of the synthesized PyBZ-TB-BPy CMP, exhibiting high T_{d5} and T_{d10} values of 472 and 573 °C [Figure 1d], along with a significant char yield of 74.4 wt % under a nitrogen atmosphere, indicating its robust structural integrity. The amorphous nature of PyBZ-TB-BPy CMP was confirmed by XRD analysis, as shown in Figure S5.

The synthesis of PyBZ-TB-BPy-Ru CMP as a dark brown solid [Figure 2a], along with a red solid for PyBZ-TB-BPy-Fe CMP [Figure 2b], a dark brown solid for PyBZ-TB-BPy-Co CMP [Figure 2c], and a red powder for PyBZ-TB-BPy-Ni CMP [Figure 2d], was successfully achieved through a one-pot, highly efficient Schiff-base [4 + 2] condensation reaction. This process involved the reaction of PyBZ-TB-4NH$_2$ and BPy-2CHO in the presence of Ru(CH$_3$COO)$_2$, Fe(CH$_3$COO)$_2$, Co(CH$_3$COO)$_2$, and Ni(CH$_3$COO)$_2$ within a 1,2-DCB/n-butanol/6 M AcOH solvent system under continuous stirring for 5 days. The inherent insolubility of PyBZ-TB-BPy-M CMP in both highly polar and less polar organic solvents ensures strong structural stability and long-term durability under catalytic conditions, making them highly suitable for efficient HER performance.

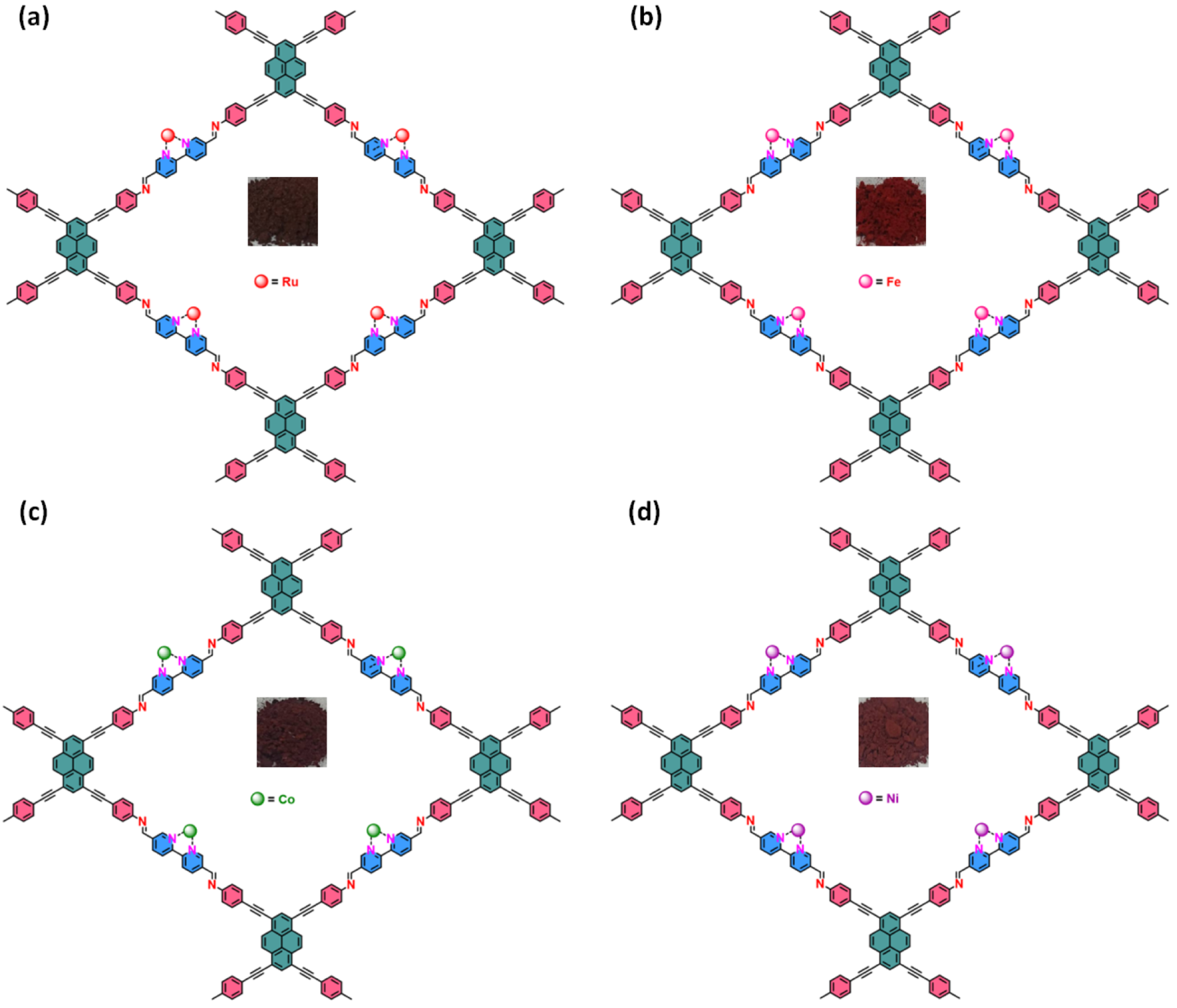

Figure 2. Structural diagram of (a) PyBZ-TB-BPy-Ru, (b) PyBZ-TB-BPy-Fe, (c) PyBZ-TB-BPy-Co, (d) PyBZ-TB-BPy-Ni CMPs.

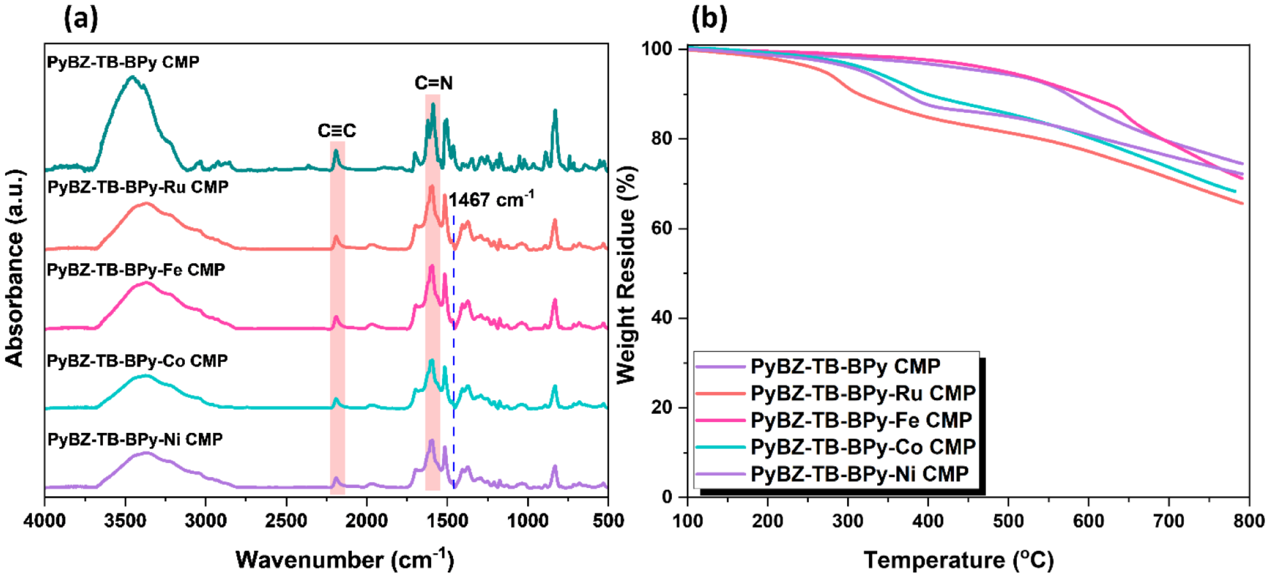

Figure 3. (a) FTIR, and (b) TGA analyses of all CMP catalysts.

As depicted in Figure 3a, all synthesized PyBZ-TB-BPy-Ru CMP, PyBZ-TB-BPy-Fe CMP, PyBZ-TB-BPy-Co CMP, and PyBZ-TB-BPy-Ni CMP exhibit distinct absorption bands characteristic of aromatic C−H (3024 cm^{-1}), C = N (1595 cm^{-1}), and Ar C = C (1512 cm^{-1}) units, confirming the successful formation of the conjugated framework. Notably,

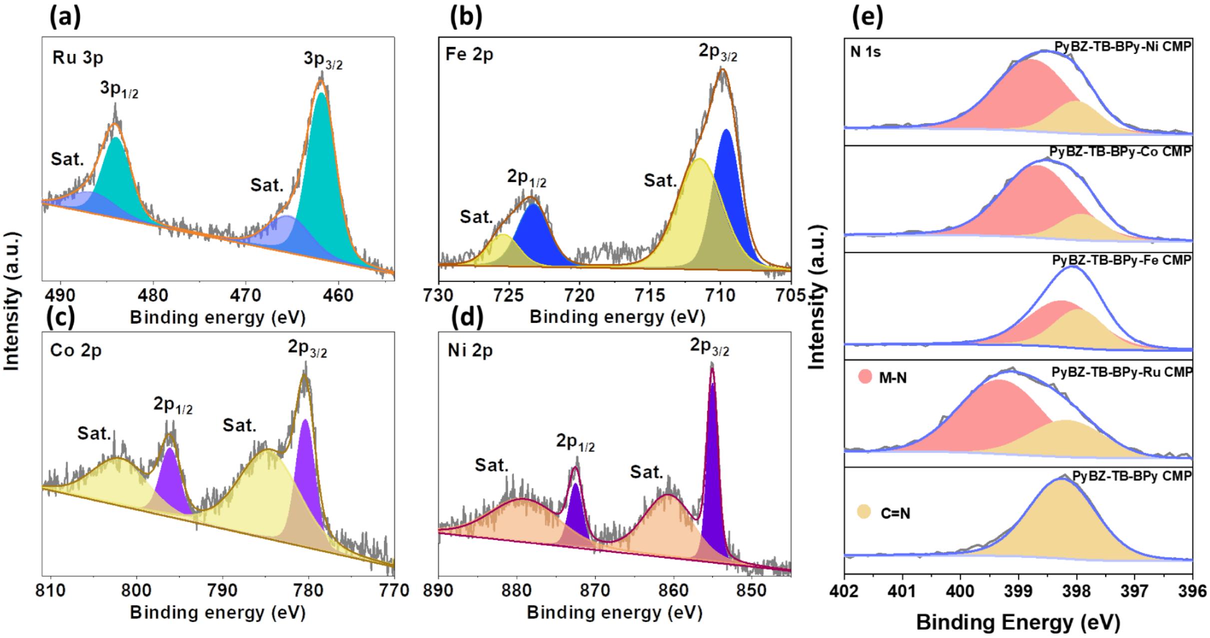

Figure 4. (a) Ru 3p spectra of PyBZ-TB-BPy CMP, (b) Fe 2p spectra of PyBZ-TB-BPy-Fe CMP, (c) Co 2p spectra of PyBZ-TB-BPy-Co CMP, (d) Ni 2p spectra of PyBZ-TB-BPy-Ni CMP, (e) N 1s spectra of all CMP catalysts.

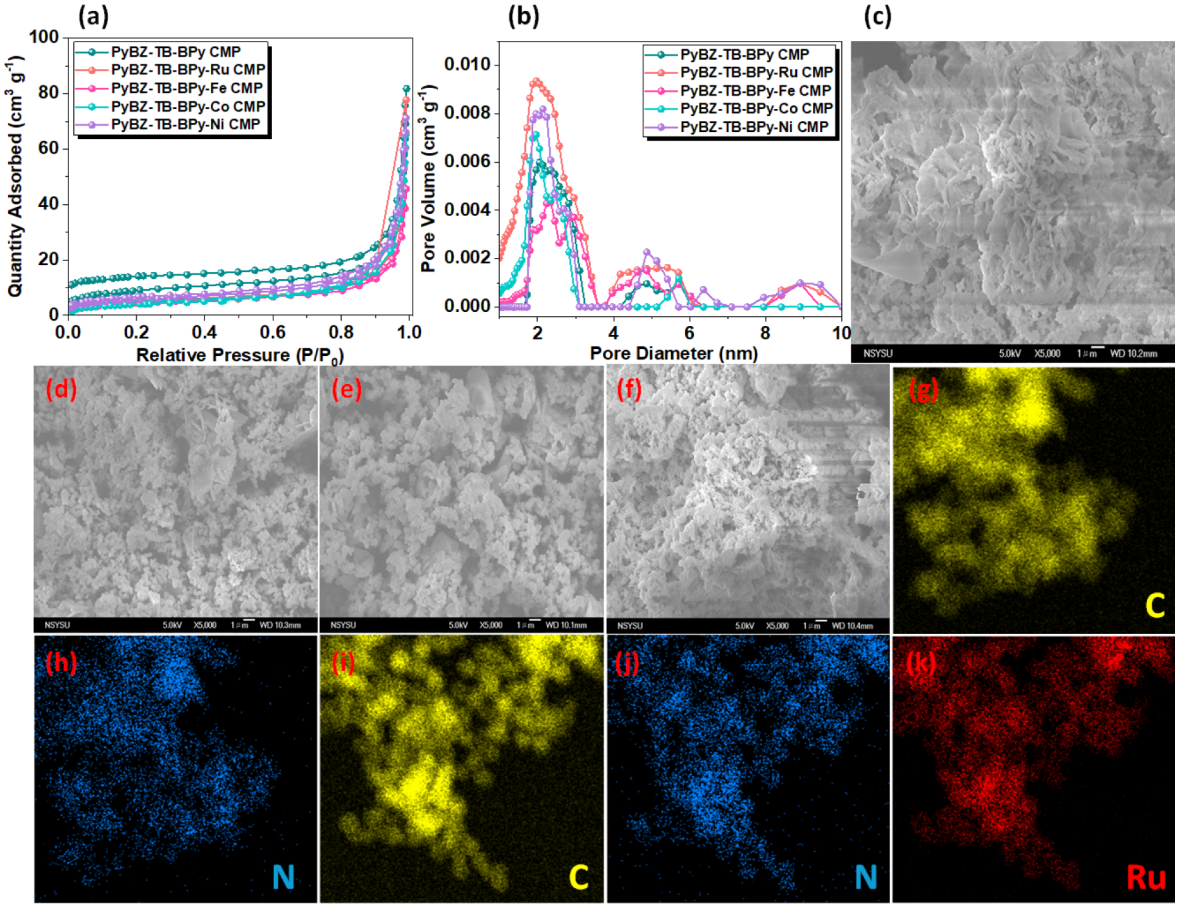

Figure 5. (a) N_2 adsorption/desorption isotherms, and (b) pore size of all CMP catalysts. (c-f) SEM images of (c) PyBZ-TB-BPy CMP, (d) PyBZ-TB-BPy-Ru CMP, (e) PyBZ-TB-BPy-Ni CMP, (f) PyBZ-TB-BPy-Co CMP. (g-k) TEM-EDS images with their corresponding elemental mapping of (g, h) PyBZ-TB-BPy CMP, and (i-k) PyBZ-TB-BPy-Ru CMP [Scale bar is 1 μm].

the complete disappearance of NH_2 and CHO absorption bands further substantiates the effective Schiff-base condensation reaction. Intriguingly, a newly emerging peak at approximately 1467 cm^{-1} is observed across all metal-

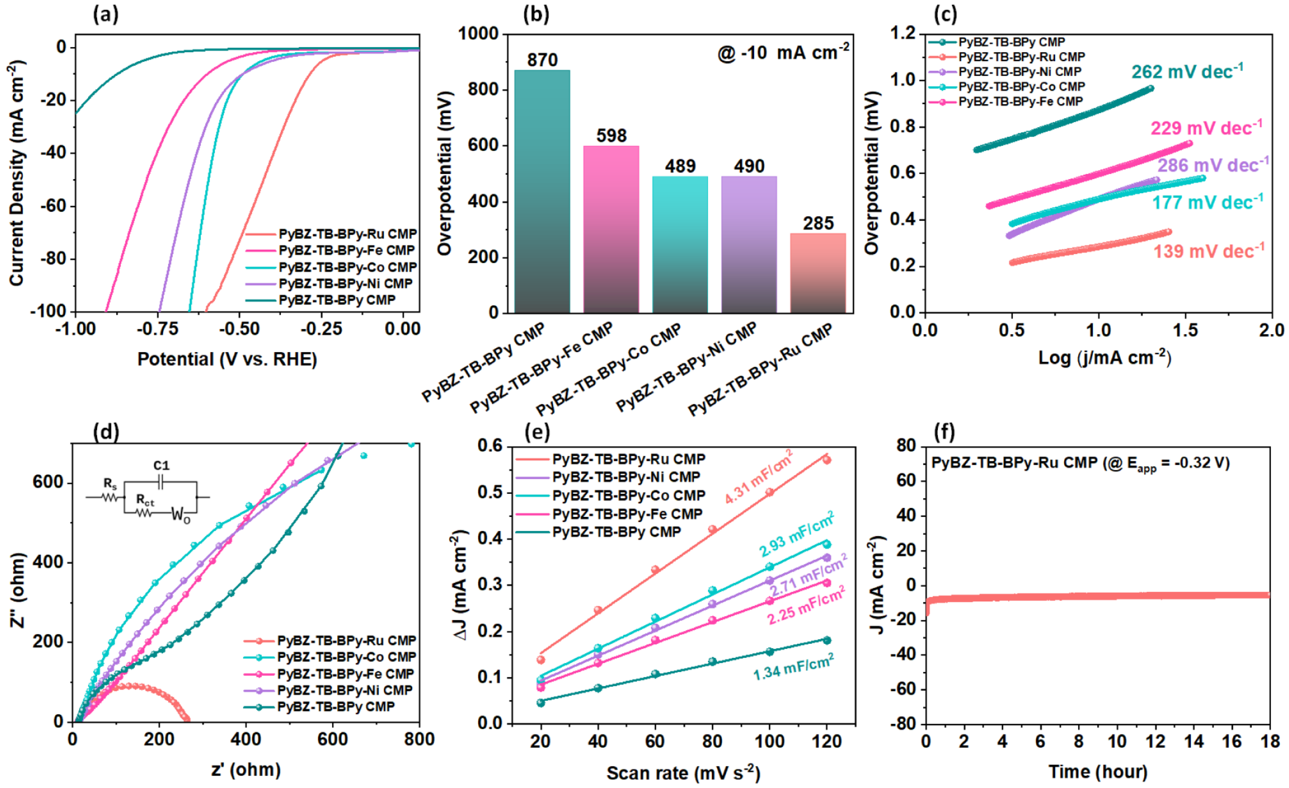

Figure 6. (a) LSV plots in 1 M KOH electrolyte, (b) Corresponding overpotential at 10 mA cm^{-2} of all CMP catalysts, (c) Tafel slope of all catalysts, (d) Nyquist plots (inset shows the equivalent circuit diagram); (e) calculated double-layer capacitance of all CMP catalysts, (f) Chronoamperometry plot of PyBZ-TB-BPy-Ru CMP in 1 M KOH electrolyte.

coordinated CMPs, attributed to C = N vibrations associated with the formation of M−N bonds between Ru, Fe, Co, and Ni and the BPy monomer, reinforcing the successful incorporation of metal ions into the polymeric network.[63] The thermal stability of all metal-coordinated PyBZ-TB-BPy CMPs was systematically evaluated, as illustrated in Figure 3b. The analysis revealed exceptional thermal resistance, with T_{d10} values recorded at 313, 590, 398, and 371 °C for PyBZ-TB-BPy-Ru CMP, PyBZ-TB-BPy-Fe CMP, PyBZ-TB-BPy-Co CMP, and PyBZ-TB-BPy-Ni CMP, respectively. Additionally, these materials demonstrated high char yields, measured at 65.6, 71.2, 68.3, and 72.2 wt %, respectively, underscoring their remarkable thermal robustness and structural integrity under elevated temperatures.

To validate the coordination of pyridinic nitrogen with metal ions, X-ray photoelectron spectroscopy (XPS) was systematically performed on PyBZ-TB-BPy CMP and PyBZ-TB-BPy-M CMP (*M* = Ru, Fe, Co, Ni). The XPS survey spectra [Figures S6 and S7] distinctly exhibit the characteristic peaks of C and N elements in the PyBZ-TB-BPy CMP and C, N, and Ru elements in PyBZ-TB-BPy-Ru CMP. Likewise, the XPS survey spectra of PyBZ-TB-BPy-Fe, PyBZ-TB-BPy-Co, and PyBZ-TB-BPy-Ni CMPs reveal the presence of Fe, Co, and Ni, along with C and N, confirming successful metal coordination [Figures S8−S10]. Additionally, the XPS profiles of all synthesized microporous PyBZ-TB-BPy-Ru CMP and PyBZ-TB-BPy-M CMP exhibited a distinct oxygen (O) peak, which is attributed to the adsorption of moisture from the ambient environment.[64] Furthermore, the high-resolution Ru 3p spectrum [Figure 4a] displays two prominent peaks corresponding to Ru 3p$_{3}$/$_{2}$ and 3p$_{1}$/$_{2}$, along with their associated satellite signals. The deconvoluted peaks at 461.9 and 484.2 eV indicate that Ru exists in the +2 oxidation state, confirming its successful incorporation into the PyBZ-TB-BPy CMP framework. In addition, high-resolution XPS spectra were obtained for the 2p orbitals of Fe, Co, and Ni in the corresponding PyBZ-TB-BPy-M CMP samples (*M* = Fe, Co, Ni). As shown in Figure 4b,d, the intense peaks at 709.6 and 723.3 eV for Fe^{2+}, 780.4 and 796.0 eV for Co^{2+}, and 855.1 and 872.4 eV for Ni^{2+}, each accompanied by characteristic satellite peaks, strongly support the presence of metal coordination and confirm the structural integrity of the synthesized materials. The high-resolution XPS N 1s spectra of PyBZ-TB-BPy-M CMP (*M* = Ru, Fe, Co, Ni) [Figure 4e] illustrate a significant transformation in the nitrogen bonding environment following metal ion coordination. As shown in Figure 4e, PyBZ-TB-BPy-Ru CMP exhibits a distinct peak at 399.3 eV, in addition to a well-defined C = N peak at 398.2 eV. This shift to higher binding energies indicates the effective coordination of nitrogen with Ru ions.[65]

The porosity of PyBZ-TB-BPy CMP and its metal-coordinated derivatives (PyBZ-TB-BPy-M CMPs) was systematically analyzed through N_2 adsorption−desorption measurements at 77 K [Figure 5a,b]. The specific surface areas, determined using the Brunauer−Emmett−Teller (BET) method, were measured as follows: PyBZ-TB-BPy CMP (31.2 m^{2} g^{-1}), PyBZ-TB-BPy-Ru CMP (19.3 m^{2} g^{-1}), PyBZ-TB-BPy-Fe CMP (16.4 m^{2} g^{-1}), PyBZ-TB-BPy-Co CMP (18 m^{2} g^{-1}), and PyBZ-TB-BPy-Ni CMP (20.3 m^{2} g^{-1}) [Figure 5a]. Additionally, pore size distribution analysis, performed using nonlocal density functional theory (NLDFT), revealed that PyBZ-TB-BPy-Ru CMP, PyBZ-TB-BPy-Fe CMP, PyBZ-TB-BPy-Co CMP, and PyBZ-TB-BPy-Ni CMP possess pores centered around 1.95 nm, which are smaller compared to the noncoordinated PyBZ-TB-BPy CMP [Figure 5b].

This reduction in pore size and surface area can be attributed to the incorporation and coordination of transition metals (Ru, Fe, Co, and Ni) within the PyBZ-TB-BPy CMP framework, leading to a moderate decrease in porosity relative to the pristine PyBZ-TB-BPy CMP structure.[63] Furthermore, the surface morphology of PyBZ-TB-BPy, PyBZ-TB-BPy-Ru, PyBZ-TB-BPy-Co, and PyBZ-TB-BPy-Ni CMPs exhibits a lumpy, accumulated structure due to the aggregation of the four CMPs via π-π interactions, based on SEM measurements [Figure 5c–f]. Transmission electron microscopy (TEM) analysis [Figure S11] confirms that the layer-stacking architectures of PyBZ-TB-BPy CMP and PyBZ-TB-BPy-M CMPs (M = Ru, Fe, Co, and Ni).[66] However, TEM-EDS elemental mapping displays C and N for Py-TB-BPy CMP [Figure 5g,h] and C, N, and Ru for Py-TB-BPy-Ru CMP [Figure 5i–k] are evenly distributed in the Py-TB-BPy-Ru CMP. Figures S12–S14 show the elemental mapping of Py-TB-BPy and Py-TB-BPy-M (M = Fe, Co, Ni), which describes the uniform distribution of elements over the sample.

Electrocatalysis of PyBZ-TB-BPy CMP, PyBZ-TB-BPy-Ru CMP, PyBZ-TB-BPy-Fe CMP, PyBZ-TB-BPy-CO CMP, and PyBZ-TB-BPy-Ni CMP for HER. The electrocatalytic performance of PyBZ-TB-BPy CMP, PyBZ-TB-BPy-Ru CMP, PyBZ-TB-BPy-Fe CMP, PyBZ-TB-BPy-Co CMP, and PyBZ-TB-BPy-Ni CMP were systematically evaluated using a conventional three-electrode setup in an alkaline electrolyte (1 M KOH). To fabricate working electrodes, catalyst ink was applied to a glassy carbon electrode (GCE) using a drop-casting technique. To assess the hydrogen evolution reaction (HER) activity, linear sweep voltammetry (LSV) was conducted for PyBZ-TB-BPy CMP and its metal-coordinated derivatives (Py-TB-BPy-M CMP, where M = Ru, Fe, Co, Ni) under alkaline conditions [Figure 6a]. As illustrated in Figure 6b, the pristine PyBZ-TB-BPy CMP exhibited a relatively high overpotential of 870 mV to achieve a 10 mA cm^{-2}, indicating limited intrinsic HER activity. However, upon metal coordination with PyBZ-TB-BPy CMP, the electrocatalytic performance was significantly enhanced, confirming that the incorporated metal centers function as the primary active sites for HER. Among the metal-coordinated PyBZ-TB-BPy CMPs, PyBZ-TB-BPy-Ru CMP demonstrated the most remarkable catalytic activity, requiring only 285 mV to reach 10 mA cm^{-2}. This was followed by PyBZ-TB-BPy-Co CMP (489 mV), PyBZ-TB-BPy-Ni CMP (490 mV), and PyBZ-TB-BPy-Fe CMP (598 mV); respectively. Furthermore, PyBZ-TB-BPy-Ru CMP exhibited superior performance even at higher current densities, as shown in Figure 6a. It achieved an overpotential of 427 mV at 50 mA cm^{-2} and 605 mV at 100 mA cm^{-2}, demonstrating excellent catalytic efficiency under increased reaction rates. More interestingly, these values compare favorably with state-of-the-art CMP and covalent organic framework (COF)-based electrocatalysts reported in the literature (Table S1), highlighting the efficiency of Ru coordination in enhancing HER activity. Beyond overpotential, the Tafel slope [Figure 6c] provides critical insight into the intrinsic catalytic kinetics of electrocatalysts. The Tafel slope of Py-TB-BPy-Ru was determined to be 139 mV dec^{-1}, indicating that the HER follows the Volmer step as the rate-determining step.[67] In contrast, the Tafel slopes of PyBZ-TB-BPy-Fe CMP, PyBZ-TB-BPy-Co CMP, PyBZ-TB-BPy-Ni CMP, and PyBZ-TB-BPy CMP were measured at 229, 177, 286, and 262 mV dec^{-1}, respectively, suggesting that Ru coordination significantly enhances reaction kinetics compared to the other metal-incorporated systems. The lower Tafel slope observed for PyBZ-TB-BPy-Ru CMP signifies improved electron transfer efficiency and a more favorable HER pathway.[68] The Tafel slope of PyBZ-TB-BPy-Ru CMP exceeds 120 mV dec^{-1}, which suggests the involvement of additional side processes. These could involve surface reduction processes at the catalyst interface or electrochemical H_2 absorption, potentially influencing the overall HER kinetics.[68] In addition to overpotential and kinetic parameters, charge transfer resistance (R_{ct}) plays an influential role in identifying the overall electrocatalytic performance (OEP). Electrochemical impedance spectroscopy (EIS) was employed to evaluate charge transfer kinetics at the electrode–electrolyte interface. As depicted in Figure 6d, the Nyquist plot revealed that PyBZ-TB-BPy-Ru CMP exhibited a significantly reduced semicircle at an overpotential of 280 mV compared to PyBZ-TB-BPy CMP and the other metal-coordinated CMPs (PyBZ-TB-BPy-Fe CMP, PyBZ-TB-BPy-Co CMP and PyBZ-TB-BPy-Ni CMP) indicating superior charge transfer efficiency. The extracted R_{ct} value for PyBZ-TB-BPy-Ru CMP was calculated to be 245 Ω, which is markedly lower than that of the other systems, confirming its enhanced electrical conductivity and improved charge transport properties.

To investigate the double-layer behavior at the electrode–electrolyte interface, the double-layer capacitance (C_{dl}) serves as a crucial parameter. Cyclic voltammetry (CV) measurements of PyBZ-TB-BPy CMP, PyBZ-TB-BPy-Ru CMP, PyBZ-TB-BPy-Fe CMP, PyBZ-TB-BPy-Co CMP, and PyBZ-TB-BPy-Ni CMP were conducted in the nonfaradaic region at varying scan rates [Figures S15–S19], and the C_{dl} values were subsequently determined from the slope of the ΔJ versus scan rate plot. As shown in Figure 6e, the calculated C_{dl} for PyBZ-TB-BPy CMP was 1.34 mF cm^{-2}. Notably, PyBZ-TB-BPy-Ru CMP exhibited a significantly higher C_{dl} value of 4.31 mF cm^{-2}, surpassing those of PyBZ-TB-BPy-Fe CMP (2.25 mF cm^{-2}), PyBZ-TB-BPy-Co CMP (2.93 mF cm^{-2}), and PyBZ-TB-BPy-Ni CMP (2.71 mF cm^{-2}). To further quantify the electrochemically active sites available for HER, the electrochemical active surface area (ECSA) was evaluated. The ECSA values for PyBZ-TB-BPy-Ru CMP, PyBZ-TB-BPy-Fe CMP, PyBZ-TB-BPy-Co CMP, PyBZ-TB-BPy-Ni CMP, and PyBZ-TB-BPy CMP were determined to be 107.75, 56.25, 73.25, 67.75, and 33.5 cm^2, respectively. These results indicate that PyBZ-TB-BPy-Ru CMP possesses the highest electrochemically active surface area, thereby providing a greater number of accessible catalytic sites for HER intermediates. This increased surface exposure is expected to enhance reaction kinetics and overall catalytic efficiency. Long-term electrochemical durability is a critical parameter in assessing catalyst performance, which was evaluated using chronoamperometric (CA) measurements. As illustrated in Figure 6f, PyBZ-TB-BPy-Ru CMP exhibited minimal changes in current density over 18 h of continuous HER under alkaline conditions at a constant potential. Chronoamperometric measurements in 1 M KOH (Figure S20) show that all samples, PyBZ-TB-BPy-CMP and its Fe, Co, and Ni variants, exhibited stable current densities over 18 h, indicating good HER operational stability.

Density functional theory (DFT) calculation was conducted on PyBZ-TB-BPy-M CMP (M = Ru, Fe, Co, Ni) to illuminate their geometric arrangement and electronic properties, providing greater insight into their electrochemical HER

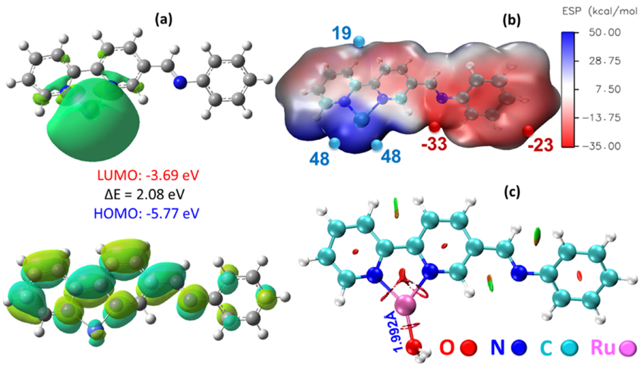

Figure 7. (a) The HOMO and LUMO isosurface maps of a model structure of the PyBZ-TB-BPy-Ru CMP along with their energies calculated at the M06-D3/def2-SVP level, (b) Molecular electrostatic potential (MESP) colored surface map with ESP surface maxima and minima (in kcal/mol) of the PyBZ-TB-BPy-Ru CMP, (c) The geometry and noncovalent interactions of water adsorbed on the surface of the PyBZ-TB-BPy-Ru CMP.

activity in an alkaline electrolyte. The highest occupied molecular orbital (HOMO) and lowest unoccupied molecular orbital (LUMO) energies, along with their corresponding isosurface maps, were computed using the M06-D3 functional with the def2-SVP basis set. As depicted in Figure 7a, the HOMO−LUMO isosurface maps of PyBZ-TB-BPy-Ru CMP reveal that the HOMO is delocalized across the entire conjugated framework, with noticeable contributions from the *d*-orbitals of the Ru center. In contrast, the LUMO predominantly comprises the vacant *d*-orbitals of the metal, highlighting its role in electron acceptance. Since HER under alkaline conditions involves the initial adsorption and dissociation of water molecules to generate reactive hydrogen intermediates (H*), a process often considered the rate-determining step, identifying optimal adsorption sites within the molecular framework is essential. To this end, molecular electrostatic potential (MESP) analysis was performed on PyBZ-TB-BPy-Ru CMP to numerically map its electrophilic and nucleophilic regions, thereby identifying the most reactive sites within the structure. As illustrated in Figure 7b, the MESP map visualizes regions of negative and positive potential, represented by red and blue areas, respectively. The MESP analysis of PyBZ-TB-BPy-Ru CMP reveals that the most electrophilic region is localized around the Ru metal center, exhibiting a positive potential of 48 kcal/mol. Furthermore, the adsorption energies (E_{ads}) for water molecules on the PyBZ-TB-BPy CMP surface were computed at the same theoretical level using the relation:

$$E_{ads} = E_{polymer-H_2O} - E_{polymer} - E_{H_2O}$$

From the adsorption study of water on the PyBZ-TB-BPy-Ru CMP surface [Figure 7c], it is evident that the lone pair of the oxygen atom in the water molecule interacts with the vacant *d*-orbitals of the Ru center, which represents the most electrophilic region, forming a coordinated bond. The calculated metal−oxygen bond distances were determined as 1.992 Å for Ru, 1.993 Å for Co, 2.002 Å for Ni, and 2.231 Å for Fe. These values indicate that PyBZ-TB-BPy-Ru CMP exhibits the strongest water adsorption affinity among the studied metal-coordinated CMPs. Additionally, the computed adsorption energies for water on PyBZ-TB-BPy-M CMP (*M* = Ru, Fe, Co, Ni) were found to be −30.1, −18.7, −30.0, and −27.8 kcal/mol for Ru, Fe, Co, and Ni, respectively. The higher adsorption energy of Ru suggests a more favorable interaction with water, thereby facilitating the crucial water adsorption step in the HER process and further enhancing its catalytic performance.

■ CONCLUSIONS

In this study, we successfully synthesized a novel electrocatalyst PyBZ-TB-BPy CMP via a Schiff base reaction between PyBZ-TB-4NH$_2$ and BPy-2CHO as building units, which are precursors, and then further developed its metal-coordinated derivatives (PyBZ-TB-BPy-M CMP) through a one-pot method. The incorporation of metal centers into the PyBZ-TB-BPy CMP framework endowed PyBZ-TB-BPy-M CMP with abundant catalytically active sites and microporous architecture, both of which considerably enhanced HER performance compared to pristine PyBZ-TB-BPy CMP. The electrochemical analysis demonstrated that PyBZ-TB-BPy-Ru CMP exhibited outstanding catalytic activity, characterized by a remarkably minimal overpotential of 285 mV at 10 mA cm^{-2}, a small Tafel slope of 139 mV dec^{-1}, the highest C_{dl} of 4.31 mF cm^{-2}, and a low R_{ct} of 245 Ω. These results highlight their superior HER performance compared to other metal-coordinated CMPs (PyBZ-TB-BPy-Fe CMP, PyBZ-TB-BPy-Co CMP, and PyBZ-TB-BPy-Ni CMP). Moreover, PyBZ-TB-BPy-Ru CMP exhibited excellent electrochemical stability, maintaining catalytic activity for 18 h in chronoamperometric tests, further demonstrating its viability as a robust HER electrocatalyst. Additionally, the Fe, Co, and Ni-coordinated PyBZ-TB-BPy CMP also exhibited improved HER activity relative to the uncoordinated PyBZ-TB-BPy CMP, reinforcing the significance of metal coordination in tuning catalytic properties. Finally, PyBZ-TB-BPy-Ru CMP exhibits overpotentials approaching 10 mA cm^{-2}, comparable to or exceeding those of the most advanced porous polymer-based catalysts. This study introduces a highly effective approach for economical water splitting (WS). Future investigations will prioritize optimizing the scalability of PyBZ-TB-BPy-based CMPs to facilitate real-world applications.

■ ASSOCIATED CONTENT

SI Supporting Information

The Supporting Information is available free of charge at https://pubs.acs.org/doi/10.1021/acsaem.5c00992.

> Electrochemical measurements; schematic scheme for the synthesis of PyBZ-TB-4NH$_2$, PyBZ-TB-BPy-Ru CMP, PyBZ-TB-BPy-Fe CMP, PyBZ-TB-BPy-Co CMP, and PyBZ-TB-BPy-Ni CMP; FTIR, NMR, and TGA data of PyBZ-TB-4NH$_2$; XRD and XPS profiles of PyBZ-TB-BPy CMP; XPS, TEM-EDX mapping, and CV profiles of PyBZ-TB-BPy-Ru CMP, PyBZ-TB-BPy-Fe CMP, PyBZ-TB-BPy-Co CMP, and PyBZ-TB-BPy-Ni CMP; chronoamperometry plots of PyBZ-TB-BPy CMP, PyBZ-TB-BPy-Fe CMP, PyBZ-TB-BPy-Co CMP, and PyBZ-TB-BPy-Ni CMP in 1 M KOH electrolyte; and comparison of the electrocatalytic performance of PyBZ-TB-BPy CMP, PyBZ-TB-BPy-Ru CMP, PyBZ-TB-BPy-Fe CMP, PyBZ-TB-BPy-Co CMP, and PyBZ-TB-BPy-Ni CMP-based materials with other

reported electrocatalysts for the hydrogen evolution reaction (HER) (PDF)

AUTHOR INFORMATION

Corresponding Authors

Mohamed Gamal Mohamed − *Department of Materials and Optoelectronic Science, Center for Functional Polymers and Supramolecular Materials, National Sun Yat-Sen University, Kaohsiung 804, Taiwan; Department of Chemistry, Faculty of Science, Assiut University, Assiut 71515, Egypt;* orcid.org/0000-0003-0301-8372; Email: mgamal.eldin34@gmail.com

Shiao-Wei Kuo − *Department of Materials and Optoelectronic Science, Center for Functional Polymers and Supramolecular Materials, National Sun Yat-Sen University, Kaohsiung 804, Taiwan; Department of Medicinal and Applied Chemistry, Kaohsiung Medical University, Kaohsiung 807, Taiwan;* orcid.org/0000-0002-4306-7171; Email: kuosw@faculty.nsysu.edu.tw

Authors

Tapomay Mondal − *Department of Materials and Optoelectronic Science, Center for Functional Polymers and Supramolecular Materials, National Sun Yat-Sen University, Kaohsiung 804, Taiwan;* orcid.org/0009-0002-3355-9487

Ahmed A. K. Mohamed − *Department of Chemistry, Faculty of Science, Assiut University, Assiut 71515, Egypt*

Complete contact information is available at:
https://pubs.acs.org/10.1021/acsaem.5c00992

Author Contributions

[#]T.M. and M.G.M. contributed equally.

Notes

The authors declare no competing financial interest.

ACKNOWLEDGMENTS

This study was supported financially by the National Science and Technology Council, Taiwan, under contracts NSTC 113-2223-E-110-001- and 113-2221-E-110-012-MY3. The authors thank the staff at National Sun Yat-sen University for their assistance with the TEM (ID: EM022600) experiments. The authors thank the staff at National Sun Yat-sen University for their assistance with the TEM (ID: EM022600) experiments.

REFERENCES

(1) Shakun, J. D.; Clark, P. U.; He, F.; Marcott, S. A.; Mix, A. C.; Liu, Z.; Otto-Bliesner, B.; Schmittner, A.; Bard, E. Global warming preceded by increasing carbon dioxide concentrations during the last deglaciation. *Nature* **2012**, *484*, 49−54.

(2) Wang, J.; Azam, W. Natural resource scarcity, fossil fuel energy consumption, and total greenhouse gas emissions in top emitting countries. *Geosci. Front.* **2024**, *15*, 101757.

(3) Bhatti, U. A.; Bhatti, M. A.; Tang, H.; Syam, M. S.; Awwad, E. M.; Sharaf, M.; Ghadi, Y. Y. Global production patterns: Understanding the relationship between greenhouse gas emissions, agriculture greening and climate variability. *Environ. Res.* **2024**, *245*, 118049.

(4) Samy, M. M.; Mohamed, M. G.; Sharma, S. U.; Chaganti, S. V.; Lee, J. T.; Kuo, S. W. An Ultrastable Tetrabenzonaphthalene-Linked conjugated microporous polymer functioning as a high-performance electrode for supercapacitors. *J. Taiwan Inst. Chem. Eng.* **2024**, *158*, 104750.

(5) Chang, S. Y.; Elewa, A. M.; Mohamed, M. G.; Mekhemer, I. M. A.; Samy, M. M.; Zhang, K.; Chou, H. H.; Kuo, S. W. Rational design and synthesis of bifunctional Dibenzo [g,p] chrysene-based conjugated microporous polymers for energy storage and visible light-driven photocatalytic hydrogen evolution. *Mater. Today Chem.* **2023**, *33*, 101680.

(6) Ram, M.; Aghahosseini, A.; Breyer, C. Job creation during the global energy transition towards 100% renewable power system by 2050. *Technol. Forecast. Soc. Change* **2020**, *151*, 119682.

(7) Suremann, N. F.; McCarthy, B. D.; Gschwind, W.; Kumar, A.; Johnson, B. A.; Hammarström, L.; Ott, S. Molecular Catalysis of Energy Relevance in Metal-Organic Frameworks: From Higher Coordination Sphere to System Effects. *Chem. Rev.* **2023**, *123*, 6545−6611.

(8) Pitchaimani, J.; Ni, S. F.; Dang, L. Metal dithiolene complexes in olefin addition and purification, small molecule adsorption, H_2 evolution and CO_2 reduction. *Coord. Chem. Rev.* **2020**, *420*, 213398.

(9) Su, L.; Luo, L.; Song, H.; Wu, Z.; Tu, W.; Wang, Z. J.; Ye, J. Hemispherical shell-thin lamellar WS_2 porous structures composited with CdS photocatalysts for enhanced H_2 evolution. *Chem. Eng. J.* **2020**, *388*, 124346.

(10) Yuan, Y.; Pan, J.; Yin, W.; Yu, H.; Wang, F.; Hu, W.; Wang, L.; Yan, D. Effective strategies to promote Z(S)-scheme photocatalytic water splitting. *Chin. Chem. Lett.* **2024**, *35*, 108724.

(11) Liang, H.; Ren, J.; Lin, R.; Liu, Y. Alternative-fuel based vehicles for sustainable transportation: A fuzzy group decision supporting framework for sustainability prioritization. *Technol. Forecast. Soc. Change* **2019**, *140*, 33−43.

(12) Li, X.; Lei, H.; Xie, L.; Wang, N.; Zhang, W.; Cao, R. Metalloporphyrins as Catalytic Models for Studying Hydrogen and Oxygen Evolution and Oxygen Reduction Reactions. *Acc. Chem. Res.* **2022**, *55*, 878−892.

(13) Samy, M. M.; Mekhemer, I. M. A.; Mohamed, M. G.; Elsayed, M. H.; Lin, K.-H.; Chen, Y.-K.; Wu, T.-L.; Chou, H.-H.; Kuo, S.-W. Conjugated microporous polymers incorporating Thiazolo[5,4-d]-thiazole moieties for Sunlight-Driven hydrogen production from water. *Chem. Eng. J.* **2022**, *446*, 137158.

(14) Chung, W. T.; Mekhemer, I. M. A.; Mohamed, M. G.; Elewa, A. M.; EL-Mahdy, A. F. M.; Chou, H. H.; Kuo, S. W.; Wu, K. C. W. Recent advances in metal/covalent organic frameworks based materials: Their synthesis, structure design and potential applications for hydrogen production. *Coord. Chem. Rev.* **2023**, *483*, 215066.

(15) Elewa, A. M.; EL-Mahdy, A. F. M.; Elsayed, M. H.; Mohamed, M. G.; Kuo, S. W.; Chou, H. H. Sulfur-doped triazine-conjugated microporous polymers for achieving the robust visible-light-driven hydrogen evolution. *Chem. Eng. J.* **2021**, *421*, 129825.

(16) Mohamed, M. G.; Elsayed, M. H.; Li, C. J.; Hassan, A. E.; Mekhemer, I. M. A.; Musa, A. F.; Hussien, M. K.; Chen, L. C.; Chen, K. H.; Chou, H. H.; Kuo, S. W. Reticular design and alkyne bridge engineering in donor−π−acceptor type conjugated microporous polymers for boosting photocatalytic hydrogen evolution. *J. Mater. Chem. A* **2024**, *12*, 7693−7710.

(17) Sharma, S. U.; Elsayed, M. H.; Mekhemer, I. M. A.; Meng, T. S.; Chou, H. H.; Kuo, S. W.; Mohamed, M. G. Rational design of pyrene and thienyltriazine-based conjugated microporous polymers for high-performance energy storage and visible-light photocatalytic hydrogen evolution from water. *Giant* **2024**, *17*, 100217.

(18) Shi, Y.; Zhang, B. Recent advances in transition metal phosphide nanomaterials: Synthesis and applications in hydrogen evolution reaction. *Chem. Soc. Rev.* **2016**, *45*, 1529−1541.

(19) Lv, X.-W.; Tian, W.-W.; Yuan, Z.-Y. Recent advances in high-efficiency electrocatalytic water splitting systems. *Electrochem. Energy Rev.* **2023**, *6*, 23.

(20) Oluigbo, C. J.; Xie, M.; Ullah, N.; Yang, S.; Zhao, W.; Zhang, M.; Lv, X.; Xie, J. Novel one-step synthesis of nickel encapsulated carbon nanotubes as efficient electrocatalyst for hydrogen evolution reaction. *Int. J. Hydrogen Energy* **2019**, *44*, 2685−2693.

(21) Wang, J.; Xu, F.; Jin, H.; Chen, Y.; Wang, Y. Non-noble metal-based carbon composites in hydrogen evolution reaction: Fundamentals to applications. *Adv. Mater.* **2017**, *29*, 1605838.

(22) Wu, W.; Wu, Y.; Zheng, D.; Wang, K.; Tang, Z. Ni@ Ru core-shell nanoparticles on flower-like carbon nanosheets for hydrogen evolution reaction at All-pH values, oxygen evolution reaction and overall water splitting in alkaline solution. *Electrochim. Acta* **2019**, *320*, 134568.

(23) Kuang, Y.; Yang, F.; Feng, L. Advancements in Ruthenium (Ru)-Based Heterostructure Catalysts: Overcoming Bottlenecks in Catalysis for Hydrogen Evolution Reaction. *Adv. Energy Mater.* **2024**, *14*, 2402043.

(24) Xiao, Y.; Zhang, J.; Liu, T.; Xu, M.; Dong, Y.; Wang, C.-A. Constructing morphologically stable supported noble metal catalysts in heterogeneous catalysis: Mechanisms and strategies. *Nano Energy* **2024**, *129*, 109975.

(25) Wang, H.; Hou, B.; Yang, Y.; Chen, Q.; Zhu, M.; Thomas, A.; Liao, Y. Cobalt Nanocrystals Encapsulated in Heteroatom-Rich Porous Carbons Derived from Conjugated Microporous Polymers for Efficient Electrocatalytic Hydrogen Evolution. *Small* **2018**, *14*, 1803232.

(26) Chen, W. F.; Sasaki, K.; Ma, C.; Frenkel, A. I.; Marinkovic, N.; Muckerman, J. T.; Zhu, Y.; Adzic, R. R. Hydrogen-evolution catalysts based on non-noble metal nickel−molybdenum nitride nanosheets. *Angew. Chem., Int. Ed.* **2012**, *51*, 6131−6135.

(27) Das, S. K.; Chowdhury, A.; Bhunia, K.; Ghosh, A.; Chakraborty, D.; Das, M.; Kayal, U.; Modak, A.; Pradhan, D.; Bhaumik, A. Ni(II) and Cu(II) grafted porphyrin-pyrene based conjugated microporous polymers as bifunctional electrocatalysts for overall water splitting. *Electrochim. Acta* **2023**, *459*, 142553.

(28) Yang, X.; Feng, X.; Tan, H.; Zang, H.; Wang, X.; Wang, Y.; Wang, E.; Li, Y. N-Doped graphene-coated molybdenum carbide nanoparticles as highly efficient electrocatalysts for the hydrogen evolution reaction. *J. Mater. Chem. A* **2016**, *4*, 3947−3954.

(29) Liu, X.; Dai, L. Carbon-based metal-free catalysts. *Nat. Rev. Mater.* **2016**, *1*, 16064.

(30) Ji, Y. Y.; Yang, L.; Ren, X.; Cui, G. W.; Xiong, X. L.; Sun, X. P. Nanoporous CoP_3 nanowire array: Acid etching preparation and application as a highly active electrocatalyst for the hydrogen evolution reaction in alkaline solution. *ACS Sustainable Chem. Eng.* **2018**, *6*, 11186−11189.

(31) Yang, Q. J.; Liu, Y.; Yan, M.; Lei, Y.; Shi, W. D. MOF-derived hierarchical nanosheet arrays constructed by interconnected NiCo-alloy@NiCo-sulfide core-shell nanoparticles for high-performance asymmetric supercapacitors. *Chem. Eng. J.* **2019**, *370*, 666−676.

(32) Yuan, X. T.; Yin, J. W.; Liu, Z. C.; Wang, X.; Dong, C. L.; Dong, W. J.; Riaz, M. S.; Zhang, Z.; Chen, M. Y.; Huang, F. Q. Charge-transfer-promoted high oxygen evolution activity of Co@ Co_9S_8 core-shell nanochains. *ACS Appl. Mater. Interfaces* **2018**, *10*, 11565−11571.

(33) Mao, B. D.; Wang, B.; Yu, F. R.; Zhang, K. W.; Zhang, Z. Y.; Hao, J. H.; Zhong, J. B.; Liu, Y. H.; Shi, W. D. Hierarchical MoS_2 nanoflowers on carbon cloth as an efficient cathode electrode for hydrogen evolution under all pH values. *Int. J. Hydrogen Energy* **2018**, *43*, 11038−11046.

(34) Basit, A.; Mohamed, M. G.; Sharma, S. U.; Kuo, S. W. Thianthrene- and Thianthrene Tetraoxide-Functionalized Conjugated Microporous Polymers for Efficient Energy Storage. *ACS Appl. Polym. Mater.* **2024**, *6*, 12247−12260.

(35) Mekhemer, I. M. A.; Elewa, A. M.; Elsenety, M. M.; Samy, M. M.; Mohamed, M. G.; Musa, A. F.; Huang, T. F.; Wei, T. C.; Kuo, S. W.; Chen, B. H.; Yang, S. D.; Chou, H. H. Self-condensation for enhancing the hydrophilicity of covalent organic polymers and photocatalytic hydrogen generation with unprecedented apparent quantum yield up to 500 nm. *Chem. Eng. J.* **2024**, *497*, 154280.

(36) Hsiao, C. W.; Elewa, A. M.; Mohamed, M. G.; Kotp, M. G.; Chou, M. M. C.; Kuo, S. W. Designing strategically functionalized hybrid porous polymers with octavinylsilsesquioxane/dibenzo[g,p]-chrysene/benzo[c]-1,2,5-thiadiazole units for rapid removal of Rhodamine B dye from water. *Colloids Surf., A* **2024**, *699*, 134658.

(37) Zhang, W.; Zuo, H.; Cheng, Z.; Shi, Y.; Guo, Z.; Meng, N.; Thomas, A.; Liao, Y. Macroscale Conjugated Microporous Polymers: Controlling Versatile Functionalities Over Several Dimensions. *Adv. Mater.* **2022**, *34*, 2104952.

(38) Mohamed, M. G.; EL-Mahdy, A. F. M.; Kotp, M. G.; Kuo, S. W. Advances in porous organic polymers: Syntheses, structures, and diverse applications. *Mater. Adv.* **2022**, *3*, 707−733.

(39) Broicher, C.; Foit, S. R.; Rose, M.; Hausoul, P. J. C.; Palkovits, R. A Bipyridine-Based Conjugated Microporous Polymer for the Ir-Catalyzed Dehydrogenation of Formic Acid. *ACS Catal.* **2017**, *7*, 8413−8419.

(40) Luo, S.; Zeng, Z.; Zeng, G.; Liu, Z.; Xiao, R.; Xu, P.; Wang, H.; Huang, D.; Liu, Y.; Shao, B.; Liang, Q.; Wang, D.; He, Q.; Qin, L.; Fu, Y. Recent advances in conjugated microporous polymers for photocatalysis: Designs, applications, and prospects. *J. Mater. Chem. A* **2020**, *8*, 6434−6470.

(41) Mohamed, M. G.; Chen, C.-C.; Zhang, K.; Kuo, S.-W. Construction of Three-Dimensional Porous Organic Polymers with Enhanced CO_2 Uptake Performance via Solid-State Thermal Conversion from Tetrahedral Benzoxazine-Linked Precursor. *Eur. Polym. J.* **2023**, *200*, 112551.

(42) Mohamed, M. G.; Chen, T. C.; Kuo, S. W. Solid-State Chemical Transformations to Enhance Gas Capture in Benzoxazine-Linked Conjugated Microporous Polymers. *Macromolecules* **2021**, *54*, 5866−5877.

(43) Mohamed, M. G.; Samy, M. M.; Mansoure, T. H.; Li, C. J.; Li, W. C.; Chen, J. H.; Zhang, K.; Kuo, S. W. Microporous Carbon and Carbon/Metal Composite Materials Derived from Bio-Benzoxazine-Linked Precursor for CO_2 Capture and Energy Storage Applications. *Int. J. Mol. Sci.* **2022**, *23*, 347.

(44) Ejaz, M.; Mohamed, M. G.; Kuo, S. W. Solid-state chemical transformation provides a fully benzoxazine-linked porous organic polymer displaying enhanced CO_2 capture and supercapacitor performance. *Polym. Chem.* **2023**, *14*, 2494−2509.

(45) Zhang, Z.; Liao, M.; Lou, H.; Hu, Y.; Sun, X.; Peng, H. Conjugated Polymers for Flexible Energy Harvesting and Storage. *Adv. Mater.* **2018**, *30*, 1704261.

(46) Han, C.; Hu, L.; Jin, S.; Ma, J.; Jiang, J.-X.; Zhang, C. Molecular Engineering in D-π-A-A-Type Conjugated Microporous Polymers for Boosting Photocatalytic Hydrogen Evolution. *ACS Appl. Mater. Interface* **2023**, *15*, 36404−36411.

(47) Chen, J.-P.; Xie, L.-F.; Huang, W.-H.; Niu, L.; Ni, Q.-L.; Huang, T.-H.; Gui, L.-C.; Wang, X.-J. Piezocatalytic Performances of Conjugated Microporous Polymers with Donor−Acceptor Structures for Overall Water Splitting. *ACS Catal.* **2024**, *14*, 7853−7866.

(48) Xu, Y. H.; Jin, S. B.; Xu, H.; Nagai, A.; Jiang, D. L. Conjugated microporous polymers: Design, synthesis and application. *Chem. Soc. Rev.* **2013**, *42*, 8012−8031.

(49) Said, A. I.; Mohamed, M. G.; Madhu, M.; Singh, P. N.; Chaganti, S. V.; Elsayed, M. H.; Tseng, W. L.; Raymo, F. M.; Kuo, S.-W. Bifunctional luminescent conjugated microporous polymers containing BODIPY and tetraphenylethene units for highly efficient energy storage and enhanced sensing of Cu^{2+} ions. *Polymer* **2024**, *300*, 126988.

(50) Sun, Y.; Zhang, T.; Li, C.; Xu, K.; Li, Y. Compositional engineering of sulfides, phosphides, carbides, nitrides, oxides, and hydroxides for water splitting. *J. Mater. Chem. A* **2020**, *8*, 13415−13436.

(51) Ali, Z.; Mehmood, M.; Aslam, M.; Haider, M. A. In-situ grown nickel-cobalt (NiCo) alloy nanoparticles decorated on petal-like nitrogen-doped carbon spheres for efficient OER activity. *ChemistrySelect* **2022**, *7*, No. e202200196.

(52) Wang, J.; Liao, T.; Wei, Z.; Sun, J.; Guo, J.; Sun, Z. Heteroatom-doping of non-noble metal-based catalysts for electrocatalytic hydrogen evolution: An electronic structure tuning strategy. *Small Methods* **2021**, *5*, 2000988.

(53) Wang, Y.; Li, S.; Wu, X.; Zhang, J.; Feng, J.; Li, M.; Zong, S.; Yan, W. Nitrogen-Based conjugated microporous polymers for efficient Hg (II) removal from Water: Performance and mechanism. *Chem. Eng. J.* **2023**, *471*, 144659.

(54) Tantisriyanurak, S.; Duguid, H. N.; Peattie, L.; Dawson, R. Acid Functionalized Conjugated Microporous Polymers as a Reusable Catalyst for Biodiesel Production. *ACS Appl. Polym. Mater.* **2020**, *2*, 3908−3915.

(55) Luo, S.; Zeng, Z.; Wang, H.; Xiong, W.; Song, B.; Zhou, C.; Duan, A.; Tan, X.; He, Q.; Zeng, G.; et al. Recent progress in conjugated microporous polymers for clean energy: Synthesis, modification, computer simulations, and applications. *Prog. Polym. Sci.* **2021**, *115*, 101374.

(56) Wang, R.; Wang, X.; Weng, W.; Yao, Y.; Kidkhunthod, P.; Wang, C.; Hou, Y.; Guo, J. Proton/electron donors enhancing electrocatalytic activity of supported conjugated microporous polymers for CO_2 reduction. *Angew. Chem., Int. Ed.* **2022**, *61*, No. e202115503.

(57) Jia, H.; Yao, Y.; Gao, Y.; Lu, D.; Du, P. Pyrolyzed cobalt porphyrin-based conjugated mesoporous polymers as bifunctional catalysts for hydrogen production and oxygen evolution in water. *Chem. Commun.* **2016**, *52*, 13483−13486.

(58) Mousa, A. O.; Mohamed, M. G.; Lin, Z. I.; Chuang, C. H.; Chen, C. K.; Kuo, S. W. Construction of cationic conjugated microporous polymers containing pyrene units through post-cationic modification for enhanced antibacterial performance. *J. Taiwan Inst. Chem. Eng.* **2024**, *157*, 105448.

(59) Mohamed, M. G.; Sharma, S. U.; Yang, C.-H.; Samy, M. M.; Mohammed, A. A. K.; Chaganti, S. V.; Lee, J.-T.; Wei-Kuo, S. Anthraquinone-enriched conjugated microporous polymers as organic cathode materials for high-performance lithium-ion batteries. *ACS Appl. Energy Mater.* **2021**, *12*, 14628−14639.

(60) Mohamed, M. G.; Su, B.-X.; Kuo, S.-W. Robust Nitrogen-Doped Microporous Carbon via Crown Ether-Functionalized Benzoxazine-Linked Porous Organic Polymers for Enhanced CO_2 Adsorption and Supercapacitor Applications. *ACS Appl. Mater. Interfaces* **2024**, *16*, 40858−40872.

(61) Mousa, A. O.; Sharma, S. U.; Chaganti, S. V.; Mansoure, T. H.; Singh, P. N.; Ejaz, M.; Chuang, C.-H.; Lee, J.-T.; Kuo, S. W.; Mohamed, M. G. Designing strategically functionalized conjugated microporous polymers with pyrene and perylenetetracarboxylic dianhydride moieties with single-walled carbon nanotubes to enhance supercapacitive energy storage efficiency. *J. Power Sources* **2024**, *608*, 234624.

(62) Mohamed, M. G.; Chen, C.-C.; Ibrahim, M.; Mousa, A. O.; Elsayed, M. H.; Ye, Y.; Kuo, S.-W. Tetraphenylanthraquinone and Dihydroxybenzene-Tethered Conjugated Microporous Polymer for Enhanced CO_2 Uptake and Supercapacitive Energy Storage. *JACS Au.* **2024**, *4*, 3593−3605.

(63) Song, W.; Chen, S.; Ren, X.; Su, X.; Song, C.; Li, Y.; Chen, L.; Bai, F. Isomeric Covalent Organic Frameworks for High-Efficiency Photocatalytic CO_2 Reduction: Substituent Position Effect. *Small* **2025**, *21*, 2409117.

(64) Sarkar, S.; Dutta, T. K.; Mandal, B. P.; Patra, A. A porous organic polymer for symmetric sodium dual-ion batteries through an adsorption-intercalation-insertion mechanism. *Chem. Commun.* **2024**, *60*, 5010−5013.

(65) Yu, B.; Li, H.; White, J.; Donne, S.; Yi, J.; Xi, S.; Fu, Y.; Henkelman, G.; Yu, H.; Chen, Z.; et al. Tuning the catalytic preference of ruthenium catalysts for nitrogen reduction by atomic dispersion. *Adv. Funct. Mater.* **2020**, *30*, 1905665.

(66) Wang, Y.; Li, X.; Dong, X.; Zhang, F.; Lang, X. Triazine-based two dimensional porous materials for visible light-mediated oxidation of sulfides to sulfoxides with O_2. *J. Colloid Interface Sci.* **2022**, *616*, 846−857.

(67) Zhao, Y.; Liang, Y.; Wu, D.; Tian, H.; Xia, T.; Wang, W.; Xie, W.; Hu, X. M.; Tian, X.; Chen, Q. Ruthenium complex of sp^2 carbon-conjugated covalent organic frameworks as an efficient electrocatalyst for hydrogen evolution. *Small* **2022**, *18*, 2107750.

(68) Wang, A.; Cheng, L.; Zhao, W.; Shen, X.; Zhu, W. Electrochemical hydrogen and oxygen evolution reactions from a cobalt-porphyrin-based covalent organic polymer. *J. Colloid Interface Sci.* **2020**, *579*, 598−606.